Chemical Science

Accepted Manuscript

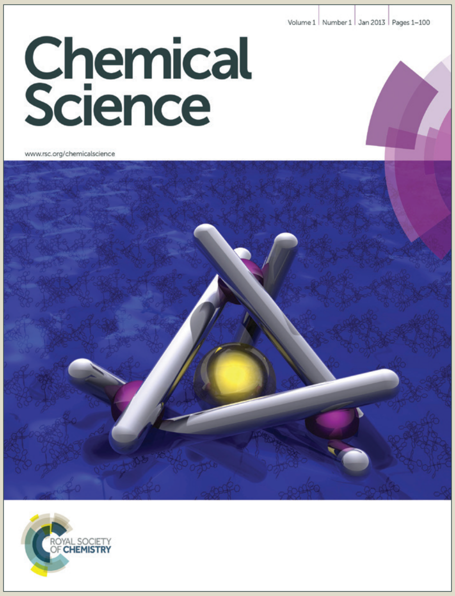

Volume 1 | Number 1 | Jan 2013 | Pages 1–100

Chemical Science

www.rsc.org/chemicalscience

ROYAL SOCIETY OF CHEMISTRY

ROYAL SOCIETY OF CHEMISTRY

www.rsc.org/chemicalscience

Insights into Structure-Photoreactivity Relationships in Well-Defined Perovskite Ferroelectric $KNbO_3$ Nanowires

Tingting Zhang,[ab] Wanying Lei,[a] Ping Liu,[c] José A. Rodriguez,[c] Jiaguo Yu,[d] Yang Qi,[b]
Gang Liu[*a] and Minghua Liu[*a]

[a]National Center for Nanoscience and Technology, Beijing 100190, China.
[b]Institute of Materials Physics and Chemistry, School of Sciences, Northeastern University, Shenyang 110004, China.
[c]Chemistry Department, Brookhaven National Laboratory, Upton, New York 11973, United States.
[d]State Key Laboratory of Advance Technology for Material Synthesis and Processing, Wuhan University of Technology, Wuhan 430070, China.

*Corresponding author: liug@nanoctr.cn; liuminghua@nanoctr.cn

Abstract

Structure-function correlations are a central theme in heterogeneous (photo)catalysis. In this study, the geometric and electronic structure of perovskite ferroelectric $KNbO_3$ nanowires with respective orthorhombic and monoclinic polymorph have been systematically addressed. By virtue of aberration-corrected scanning transmission electron microscopy, we directly visualize surface photocatalytic active sites, measure local atomic displacements at an accuracy of several picometers, and quantify ferroelectric polarization combined with first-principles calculations. The photoreactivity of the as-prepared $KNbO_3$ nanowires is assessed toward aqueous rhodamine B degradation under UV. A synergy between ferroelectric polarization and electronic structure in photoreactivity enhancement is uncovered, which account for the prominent reactivity order: orthorhombic > monoclinic. Additionally, by identifying new photocatalytic products, rhodamine B degradation pathways involving N-deethylation and conjugated structure cleavage are proposed. Our findings not only provide new insights into the structure-photoreactivity relationships in perovskite ferroelectric photocatalysts, but also have broad implications in perovskite-based water splitting and photovoltaics, among others.

Introduction

Since Fujishima and Honda discovered photocatalytic water splitting on TiO_2,[1] the past decades have seen a significant rise in light-driven pollutant abatement,[2-5] selective oxidation,[6, 7] and water splitting.[8-14] Despite tremendous progress being made, the mechanisms of photocatalysis are not yet known in detail. In the conceptual framework of heterogeneous (photo)catalysis, the mechanistic understanding of structure-function relationships is prerequisite to the rational design of efficient photocatalysts. On the other hand, semiconductor-based photocatalysis is inherently complex in that both surface structure and bulk structure of a given photocatalyst synergetically dictate the photocatalytic efficiency:[5, 15] the bulk absorbs incident photons and generates $e^{-}–h^{+}$ charge pair, while the surface harnesses available $e^{-}–h^{+}$ to catalyze target adsorbates on the photocatalytic active sites. To this end, a driving force (e.g., internal electronic field functional like a p-n junction) for facilitating the spatial separation of the $e^{-}–h^{+}$ pair is desirable.[16-21] Apparently, the complexity of photocatalysis hampers an atomistic understanding of structure-function relationships. For instance, most previous studies about internal electronic field-mediated photocatalysis are carried out on irregularly-shaped powders in which the active sites are unclear,[22-24] making it difficult to explore structure-function relationships. Only a thorough understanding of structure-function relationships in well-defined model catalysts can add new dimensions to our fundamental view of "real world" catalysis as well as rationally design catalysts at an atomic-level.[25-27] Recent advances in synthesizing nanocrystals allow for fine control of the size and shape of (photo)catalysts.[28-31] To date, a great deal of studies in nanostructured photocatalysts are focused on facet-dependent photocatalysis.[32-38] Nevertheless, the underlying synergetic effects involved in photocatalysis remain largely unexplored.

In this study, we investigated photocatalytic degradation of rhodamine B (RhB) in water (a model reaction in the removal of organic pollutants from wastewater) on one-dimensional (1D) single-crystalline potassium niobate ($KNbO_3$) nanowires (NWs) with respective orthorhombic and monoclinic polymorph. $KNbO_3$ is a typical ferroelectric perovskite (general formula ABO_3, where A is a metal, B is a second metal, and O is oxygen) with diverse emerging technological applications, including photocatalysis with the advantages of non-toxicity, cost-effectiveness and high stability under light illumination.[39, 40] In 1D nanostructures, it is possible to enhance the photoreactivity by tuning the transport of photogenerated charge carriers through quantum confinement.[41, 42] Currently, the understanding of ferroelectric materials is based primarily on theory, since few experimental techniques can be used to probe the local atomic displacements that give rise to polarization. Thank to recent progress in aberration-corrected transmission electron microscopy (TEM),[43, 44] by which it is possible to measure local polarization displacements at an accuracy of several picometers and determine surface terminations by profile imaging. Herein, by advanced aberration-corrected scanning transmission electron microscopy (STEM), we directly visualize surface photocatalytic active sites, measure local atomic displacements at an accuracy of several picometers, and quantify ferroelectric polarization combined with spin-polarized density functional theory (DFT) calculations. We uncover a novel photocatalytic synergy between ferroelectric polarization and electronic structure, which account for the prominent reactivity order: orthorhombic > monoclinic. Additionally, RhB degradation pathways involving N-deethylation and conjugated structure cleavage are proposed.

Results and discussion

Fig. 1a, b illustrate the crystal structures of monoclinic and orthorhombic $KNbO_3$ polymorph, denoted as m-$KNbO_3$ and o-$KNbO_3$, respectively. X-ray diffraction (XRD) patterns as displayed in Fig. 1c confirm the as-prepared m-$KNbO_3$ (space group *P1m1*) and o-$KNbO_3$ (space group *Bmm2,* JCPDS card 71-2171) samples with comparable crystallinity, evidenced by the full-width at half-maximum (FWHM), e.g., about 0.23° for the peak at 31.5° for m-$KNbO_3$ and o-$KNbO_3$, respectively. High-resolution XRD in the range of 44°−46° (Fig. 1d) further indicates apparent structural difference between the above two structures. Scanning electron microscopy (SEM) images (Fig. 1e, f) show well-defined elongated m- and o-$KNbO_3$ NWs. Combined SEM and atomic force microscopy (AFM) (Fig. S1†) measurements indicate that the average length, width, and height for m-$KNbO_3$ NWs is respective (1.3±0.5) μm, (106±47) nm, and (138±36) nm, while for o-$KNbO_3$ NWs is (1.2±0.4) μm, (102±27) nm, and (136±17) nm, respectively. High-resolution transmission electron microscopy (HRTEM) images (Fig. S2†) prove that m-$KNbO_3$ NWs are enclosed by {100}, {010} and {001} facets,[45] and o-$KNbO_3$ NWs are enclosed by {101} and {010} facets.[46] The growth direction of m- and o-$KNbO_3$ NWs is [100] and [101], respectively. The BET specific surface area is measured to be 4.7 and 4.8 $m^2\cdot g^{-1}$ for respective m- and o-$KNbO_3$ NWs (Table 1). The photophysical property is revealed by diffuse-reflectance UV-Vis (DRUV-Vis) spectroscopy (Fig. 2a). The bandgap (E_g) of $KNbO_3$ NWs is determined with a Tauc plot (in the inset of Fig. 2a): m- and o-$KNbO_3$ NWs possess a bandgap of 3.15 and 3.25 eV, respectively. The bandgap of o-$KNbO_3$ is similar to that reported in previous work (3.2 eV).[47] Similar with previous reports Fig. 2b shows the O *K*-edge features of X-ray absorption near-edge spectroscopy (XANES) spectra. Peak A centered at 531.4 eV is ascribed to the hybridization of O 2p with Nb 4d-t_{2g} through π* interaction. Both B and C peaks observed at respective 535.0 and 537.8 eV are attributed to the hybridization of O 2p with Nb 4d-e_g (σ* interaction) and Nb 5p (π*, σ* interaction).[48] The relative peak intensity ratio between A and C is dramatically decreased from m- to o-$KNbO_3$ NWs, suggesting that O chemical environment is different between m- and o-$KNbO_3$ NWs. High-resolution X-ray photoelectron spectroscopy (XPS) spectra (Fig. 2c) indicate that Nb $3d_{5/2}$ is ca. 206.5 and 206.6 eV for m- and o-$KNbO_3$ NWs, respectively. Fig. 2d reveals that m- and o-$KNbO_3$ NWs present similar valence band (VB) maxima (ca. 2.2 eV) and line shape, and no detectable oxygen vacancy defects exist. Since o-$KNbO_3$ NWs has a greater bandgap than m-$KNbO_3$ NWs, the conduction band (CB) minimum of o-$KNbO_3$ NWs should be raised with respect to that of m-$KNbO_3$ NWs. The above results demonstrate the intrinsic difference of geometric structure and electronic structure between m- and o-$KNbO_3$ NWs, albeit they share similar size, crystallinity and specific surface area.

To examine the geometric structure of m- and o-$KNbO_3$ NWs at an atomic level, we utilized annular-bright-field (ABF)-STEM.[49] In general, the contrast of ABF imaging depends on $Z^{1/3}$ (Z is atomic number) and light elements like O can be directly visualized at subangstrom resolution.[50] Therefore, the understanding of ABF imaging contrast in metal oxides is straightforward. Herein, the spots of black, dark grey and light grey correspond to NbO (Z_{Nb} = 41), K (Z_K = 19) and O (Z_O = 8) columns seen end-on, respectively. The representative surface structure of m- and o-$KNbO_3$ NWs is revealed by profile-view imaging (Fig. 3a, b) taken along the [010] direction. Cyan, red and purple symbols denote NbO, K and O columns, respectively. According to the corresponding line profiles (Fig. 3c, d), the spacing between NbO columns (4.02 Å and 4.04 Å) fits well to the m-$KNbO_3$ (001) and o-$KNbO_3$ (−101), respectively. The outmost surface layer of m-$KNbO_3$ (001) and o-$KNbO_3$ (−101) is NbO_2 terminated, where the exposed Nb cation (denoted as Nb_{5c}) is bonded to five oxygen anions. In general, the coordinatively unsaturated surface cations often act as active sites in heterogeneous photocatalysis.[32] Additionally, neither surface relaxations nor reconstructions are observed. Other facets like {100} and {010} of m-$KNbO_3$, {010} of o-$KNbO_3$, are also predominantly NbO_2 terminated (data not shown). The local bulk structure of $KNbO_3$ NWs is directly visualized as well. To identify the precise atomic positions from ABF images at an accuracy of several picometers and then quantitatively determine the delicate structural difference, we employed Bragg filtering and "Find Peaks" option based on Peak Pairs Analysis.[51, 52] The atomic column locations are obtained as coordinates (x, y) by fitting a two-dimensional (2D) quadratic function and calculating the maxima of the atomic column positions. The ABF imaging of m- and o-$KNbO_3$ NWs viewed along different crystallographic directions with overlaid red dots obtained by Peak Pairs Analysis in Fig. 4 clearly shows the precise atomic column positions. As schematic illustrated by representative zoom-in colour-enhanced ABF images (Fig. 4), clear atomic displacements with respect to the $KNbO_3$ cubic structure are observed.[44] For example, the zoom-in colour-enhanced ABF images in Fig. 4a present that the NbO columns shift to the lower-right and O columns shift the upper-left within the rectangles formed by four K columns. Table S1† displays the displacements of Nb atoms and O atoms along different directions, denoted as δ_{Nb} and δ_{O}, respectively. Herein, different O atoms are numbered according to the coordinates. The atomic displacements in m-$KNbO_3$ NWs of O1, O2, O3 and Nb1 are −0.12±0.05, −0.11±0.03, −0.10±0.04 and 0.05±0.03 Å along the [100] direction, 0.11±0.06, 0.10±0.04, 0.11±0.03 and −0.05±0.04 Å along the [001] direction. No detectable displacements are probed for Nb and O atoms along the [010] direction. As for o-$KNbO_3$ NWs, the atomic displacements of O1, O3, O5 and Nb1 are 0.22±0.03, 0.21±0.05, 0.21±0.04 and −0.15±0.05 Å along the [−101] direction, 0.21±0.06, 0.20±0.03, 0.21±0.05 and −0.14±0.04 Å along the [101] direction. Additionally, no detectable displacements are observed along the [010] direction for Nb and O atoms. The observed difference of atomic displacements for m- and o-$KNbO_3$ is owing to the intrinsic structural discrepancy. The atomic displacements are corroborated by spin-polarized DFT calculations as shown in Table S2 and S3†, which are in good agreement with the STEM measurements. In the $KNbO_3$ unit cell, spontaneous ferroelectric polarization (denoted as P_{sp}) arises from the displacement of the positive charge center and negative charge center. And K contribution to the total polarization is negligible owing to the essential ionic interaction between K and O.[53] P_{sp} is calculated on the basis of lattice parameters, atomic displacements and Born effective charges of the ions, while the Born effective charges are determined using spin-polarized DFT calculations.[44, 54] The results are shown in Table S2 and S3†. The vector of P_{sp} is pointed from the net negative to the net positive charge. As for m-$KNbO_3$, the local polarization is 20 $\mu C \cdot cm^{-2}$ along the <10−1> direction. In case of o-$KNbO_3$, the local polarization is 42 $\mu C \cdot cm^{-2}$ along the <001> direction. Due to the crystal size limitations, mapping domains in $KNbO_3$ NWs by STEM imaging is difficult. Nevertheless, the delicate structural variations-derived local polarization is distinct between m- and o-$KNbO_3$ NWs and expected to cause different photocatalysis. The photoreactivity of $KNbO_3$ NWs was assessed toward RhB degradation in water under UV. The reaction rate constants were calculated and the results are displayed in Fig. 5a. In the absence of $KNbO_3$, RhB degradation is negligible (data not shown). Under the identical experimental conditions, o-$KNbO_3$ NWs display photoreactivity ($k = 4.21 \times 10^{-3}$ min^{-1}) that is about two-fold as large as that of m-$KNbO_3$ NWs ($k = 2.04 \times 10^{-3}$ min^{-1}). Further, the photostability was examined and the results are shown in ESI (Fig. S3–S5†). With regard to the reaction products concerning RhB degradation, such as total organic carbon (TOC), intermediate products, and inorganic mineralization species, detailed analyses along with proposed reaction pathways are given in the ESI (Tables S4, S5 and Fig. S6–S8†).

To explore the photoreactivity difference between m- and o-$KNbO_3$ NWs, a brief overview of photocatalytic process is introduced as following. In general, semiconductor-based photocatalysis involves three steps: the photogeneration of e^-–h^+ pair, the separation and transport of e^-–h^+, and their reaching the surface and reaction with the adsorbates. In the first step, electronic structure like the bandgap of a given photocatalyst determine light absorption and the redox potentials of photo-induced charge carriers.[31] Because o-$KNbO_3$ NWs has a greater bandgap than m-$KNbO_3$ NWs, o-$KNbO_3$ NWs possess higher CB minimum than m-$KNbO_3$ NWs and thus generate more strongly reductive electrons in photocatalysis.[34] The discrepancy of electronic structure is in good agreement with structural variations between m- and o-$KNbO_3$. The key issue of the second step is the charge pair recombination. Utilizing internal electric field as a driving force is an emerging approach to suppress e^-–h^+ recombination.[18, 19] Recent photocatalytic studies on the effects of internal electric field in $BaTiO_3$,[55] ZnS,[56] AgI[4] and $BiVO_4$[57] were only qualitatively discussed. In the present study, the magnitude of local polarization for m- and o-$KNbO_3$ is determined. o-$KNbO_3$ NWs present the polarization of 42 $\mu C\cdot cm^{-2}$ along the <10−1> direction. As for m-$KNbO_3$, the polarization is 20 $\mu C\cdot cm^{-2}$ along the <10−1> direction. As such, a positive charge on the surface is produced when polarization points from the bulk to the surface, vice versa. To compensate this bound charge, both internal screening and external screening occur.[55] For internal screening, the free charge carriers in the bulk move to the opposite charged surfaces, resulting in respective downward and upward band bending on positive and negative charged surfaces as shown in Fig. 5b. The resulting band bending further provides a driving force for the spatial separation of photo-excited electrons and holes.[19] External screening refers to the adsorption of molecules like RhB. Based on the above analysis, o-$KNbO_3$ NWs exhibit more enhanced photoreactivity than m-$KNbO_3$ NWs, illustrating that the greater local polarization, the more enhanced photoreactivity. The third step is relevant to the photocatalyst surface structure. Herein, the respective density of Nb_{5c} for m-$KNbO_3$ NWs {010}, {001} and {100} is 6.14, 6.19 and 6.23 atoms·nm^{-2}, very similar to 6.14 and 6.24 atoms·nm^{-2} for {010} and {101} of o-$KNbO_3$ NW. Therefore, in this work surface structure is most likely not a leading factor in causing distinct photocatalytic performance. Considering that o-$KNbO_3$ NWs are able to generate more strongly reductive electrons than m-$KNbO_3$ counterparts under UV, we conclude that both ferroelectric polarization and electronic structure synergetically dictate the photocatalytic performance. Unlike previous studies that emphasized the effects of exposed facets[34-38] in photocatalysis, our results indicate that ferroelectric polarization dictates the photoreactivity by driving e^- and h^+ to the photocatalyst surface to trigger the photocatalytic reaction, albeit the facets of m- and o-$KNbO_3$ NWs expose comparable surface low-coordinate Nb density. That is, a unique route for directing the transport of photo-excited charge carriers and enhancing the photoreactivity.

Conclusions

In summary, with a combination of advanced ABF-STEM imaging and DFT calculations we directly probed the atomic surface structure, measured delicate atomic displacements at an accuracy of several picometers, and quantified associated local polarization in single-crystalline m- and o-$KNbO_3$ NWs with comparable size, crystallinity and specific surface area. Orthorhombic $KNbO_3$ nanowires display about two-fold as large as monoclinic counterparts toward RhB photodegradation and the underlying mechanism can be rationalized as the novel synergy of delicate atomic structural variations-derived ferroelectric polarization and electronic structure. Additionally, RhB degradation pathways are proposed, with an emphasis on N-deethylation and conjugated structure cleavage. This study not only provides a new atomic-level understanding of structure-photoreactivity relationships in perovskite ferroelectric photocatalysts, but also has broad implications in perovskite-based water splitting and photovoltaics, among others.

Figure Captions:

Fig. 1. (a) Crystal structure of m-$KNbO_3$. (b) Crystal structure of o-$KNbO_3$. (c) Powder XRD patterns of m- and o-$KNbO_3$ NWs. (d) High-resolution XRD patterns in the range of 44°−46°. (e) SEM image of m-$KNbO_3$ NWs. (f) SEM image of o-$KNbO_3$ NWs. M: m-$KNbO_3$ NWs; O: o-$KNbO_3$ NWs.

Fig. 2. (a) DRUV-Vis spectra and corresponding plots of $(\alpha h\nu)^{1/2}$ versus photon energy ($h\nu$). (b) O *K*-edge XANES spectra. (c) High-resolution XPS spectra of Nb 3d core-level. (d) Valence band spectra. M: m-$KNbO_3$ NWs; O: o-$KNbO_3$ NWs.

Fig. 3. Representative atomic-scale surface structure of m- and o-$KNbO_3$ NW by ABF-STEM profile-view imaging. (a) m-$KNbO_3$ viewed along the [010] direction (cyan: NbO, red: O, purple: K). (b) o-$KNbO_3$ viewed along the [010] direction (cyan: NbO, red: O, purple: K). (c) Corresponding line profiles showing the image intensity as a function of position in image (a) along a–a'. (d) Corresponding line profiles showing the image intensity as a function of position in image (b) along a–a'.

Fig. 4. Representative atomic-scale bulk structure of m- and o-$KNbO_3$ NWs by ABF-STEM imaging. The images are overlaid with red dots that represent atomic column positions at an accuracy of several picometers obtained by Peak Pairs Analysis. Corresponding zoom-in colour-enhanced ABF images are highlighted. (a) m-$KNbO_3$ NWs viewed along the [010] direction. (b) m-$KNbO_3$ NWs viewed along the [001] direction. (c) o-$KNbO_3$ NWs viewed along the [−101] direction. (d) o-$KNbO_3$ NWs viewed along the [010] direction. P_{sp} is the polarization.

Fig. 5. (a) Photoreactivity of m- and o-$KNbO_3$ NWs toward RhB degradation in water under UV. (b) Representative schematic illustration of charge separation in $KNbO_3$ NWs under UV and associated photocatalytic degradation of RhB. E_v is the valence band edge, E_c is the conduction band edge, P_{sp} is the polarization and E is the internal electric field.

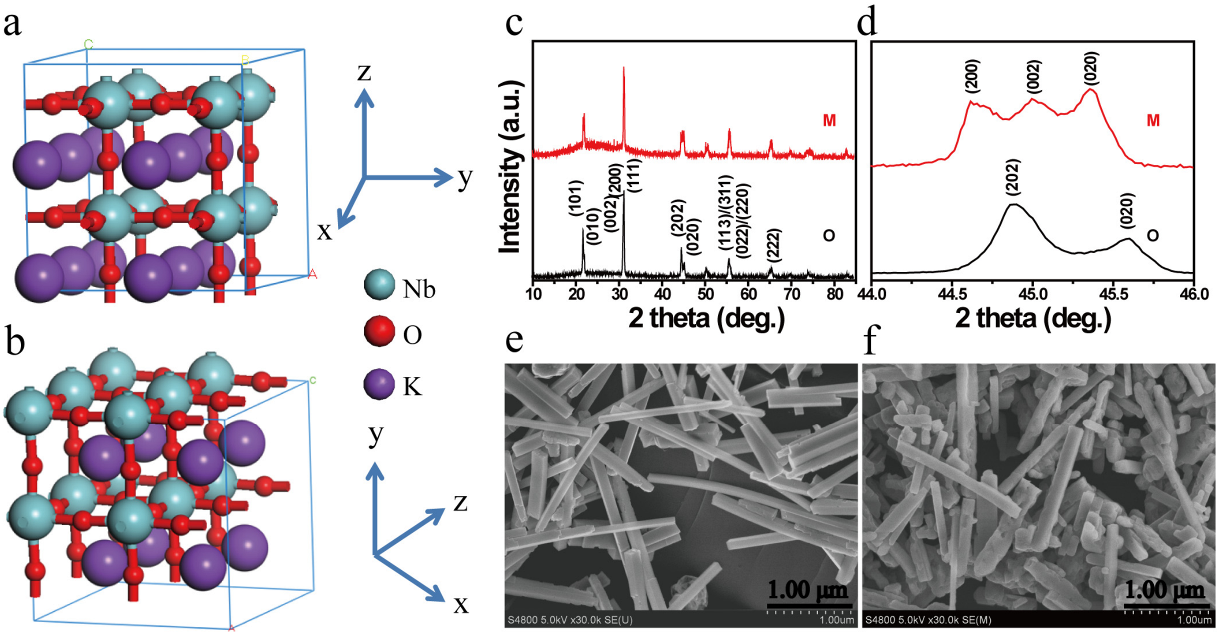

Fig. 1. (a) Crystal structure of m-$KNbO_3$. (b) Crystal structure of o-$KNbO_3$. (c) Powder XRD patterns of m- and o-$KNbO_3$ NWs. (d) High-resolution XRD patterns in the range of 44°−46°. (e) SEM image of m-$KNbO_3$ NWs. (f) SEM image of o-$KNbO_3$ NWs. M: m-$KNbO_3$ NWs; O: o-$KNbO_3$ NWs.

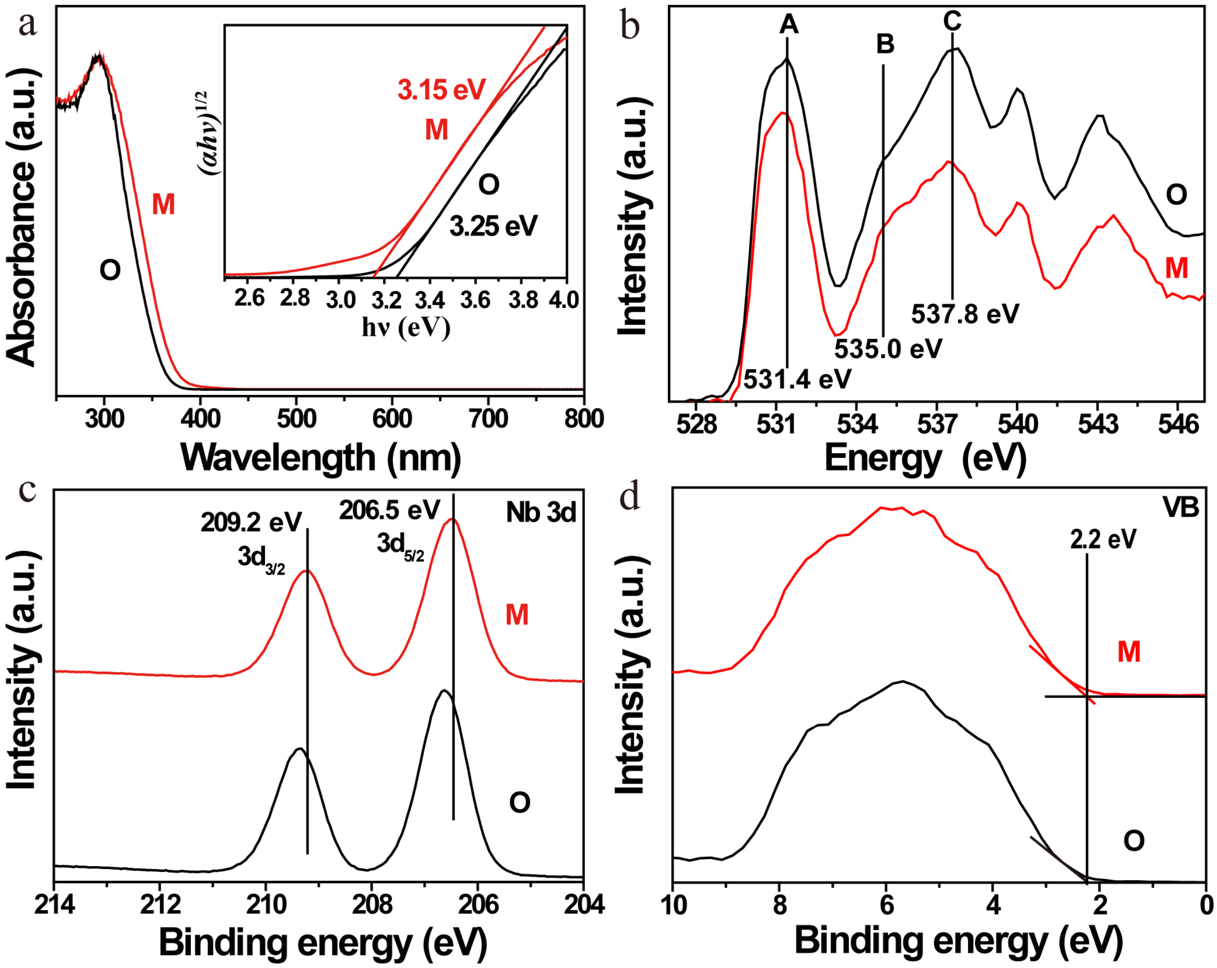

Fig. 2. (a) DRUV-Vis spectra and corresponding plots of $(\alpha h\nu)^{1/2}$ versus photon energy ($h\nu$). (b) O *K*-edge XANES spectra. (c) High-resolution XPS spectra of Nb 3d core-level. (d) Valence band spectra. M: m-$KNbO_3$ NWs; O: o-$KNbO_3$ NWs.

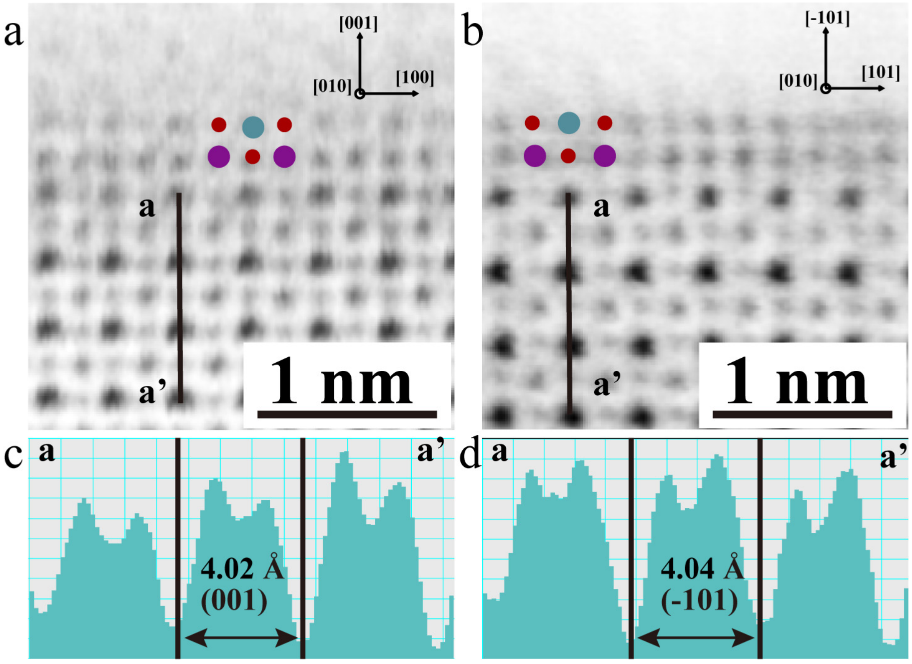

Fig. 3. Representative atomic-scale surface structure of m- and o-$KNbO_3$ NW by ABF-STEM profile-view imaging. (a) m-$KNbO_3$ viewed along the [010] direction (cyan: NbO, red: O, purple: K). (b) o-$KNbO_3$ viewed along the [010] direction (cyan: NbO, red: O, purple: K). (c) Corresponding line profiles showing the image intensity as a function of position in image (a) along a–a'. (d) Corresponding line profiles showing the image intensity as a function of position in image (b) along a–a'.

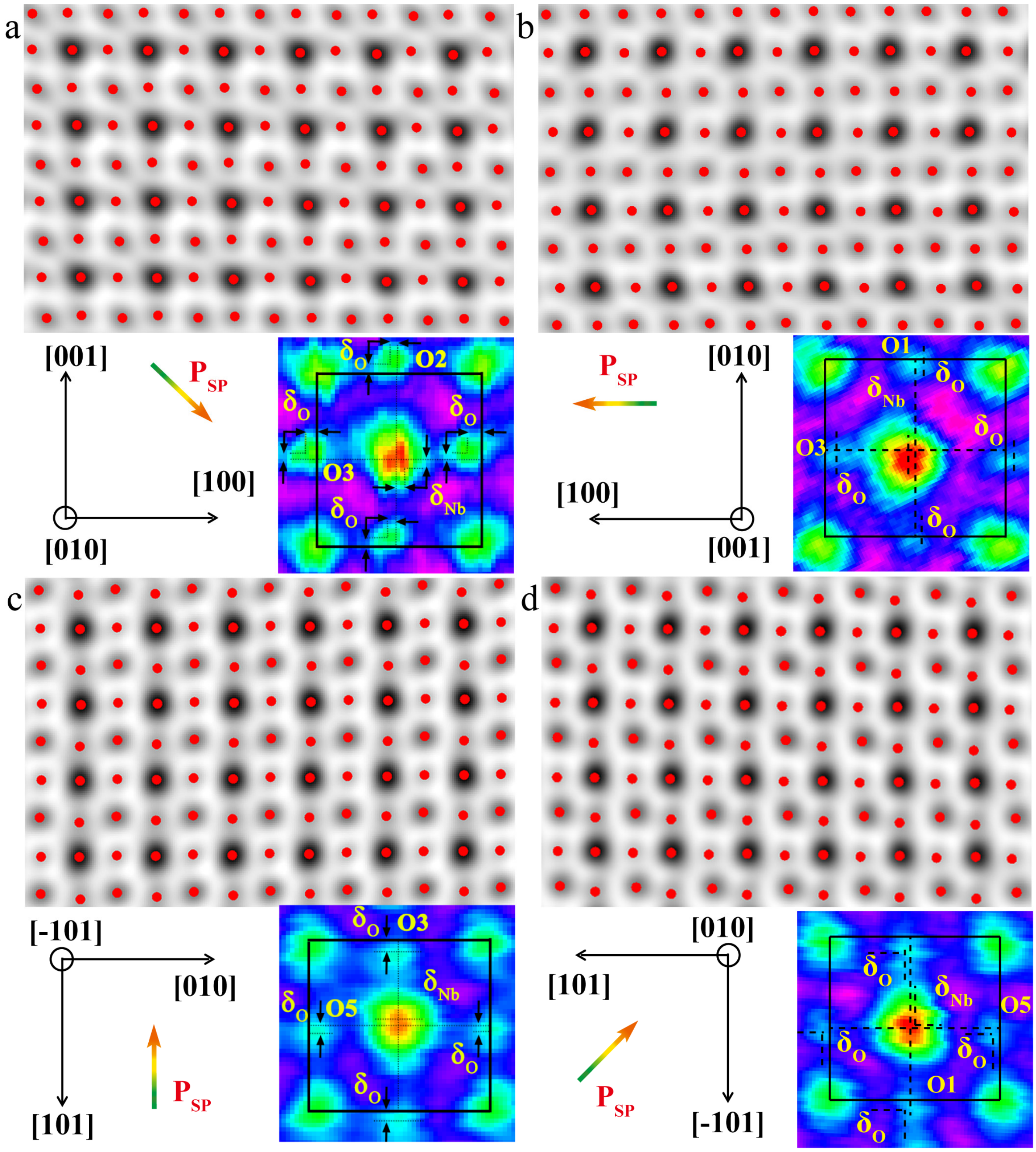

Fig. 4. Representative atomic-scale bulk structure of m- and o-$KNbO_3$ NWs by ABF-STEM imaging. The images are overlaid with red dots that represent atomic column positions at an accuracy of several picometers obtained by Peak Pairs Analysis. Corresponding zoom-in colour-enhanced ABF images are highlighted. (a) m-$KNbO_3$ NWs viewed along the [010] direction. (b) m-$KNbO_3$ NWs viewed along the [001] direction. (c) o-$KNbO_3$ NWs viewed along the [−101] direction. (d) o-$KNbO_3$ NWs viewed along the [010] direction. P_{sp} is the polarization.

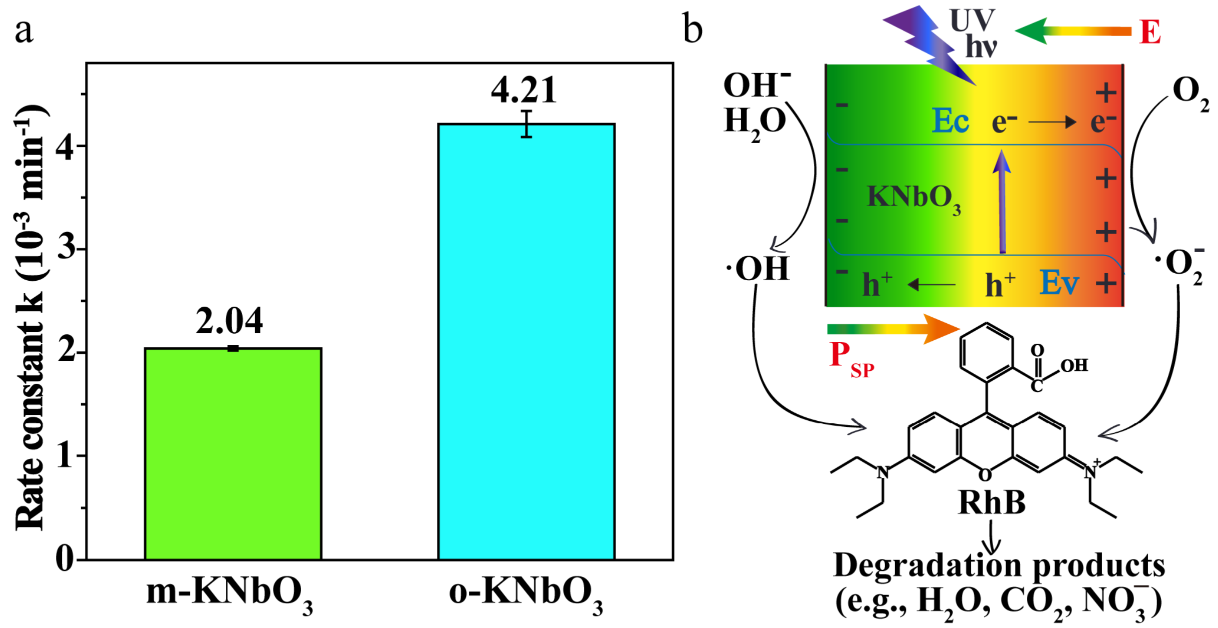

Fig. 5. (a) Photoreactivity of m- and o-$KNbO_3$ NWs toward RhB degradation in water under UV. (b) Representative schematic illustration of charge separation in $KNbO_3$ NWs under UV and associated photocatalytic degradation of RhB. E_v is the valence band edge, E_c is the conduction band edge, P_{sp} is the polarization and E is the internal electric field.

Table 1. Physicochemical properties of m- and o-$KNbO_3$ NWs.

Samples	BET specific surface area [$m^2 \cdot g^{-1}$]	Bandgap [eV]	Exposed facets	Ferroelectric polarization [$\mu C \cdot cm^{-2}$]	Density of surface low-coordinate Nb cations [$atoms \cdot nm^{-2}$]	Reaction rate constant k [$\times 10^{-3}$ min^{-1}]
m-$KNbO_3$	4.7	3.15	{010} {001} {100}	20	6.14 6.19 6.23	2.04
o-$KNbO_3$	4.8	3.25	{010} {101}	42	6.14 6.24	4.21

Associated Content

†Electronic supplementary information (ESI) available: Additional figures and tables, synthetic procedures, theoretical calculation methods, experimental details for XRD, spectroscopy (XPS, XANES and UV-vis), microscopy (AFM, SEM, HRTEM and STEM) and photocatalytic experiments.

Author Information

Corresponding Author: *liug@nanoctr.cn; liuminghua@nanoctr.cn*

Acknowledgements

We thank Prof. Jincai Zhao (Institute of Chemistry, CAS) for fruitful discussions. We also thank Prof. Jiaou Wang and Tao Lei for their help in the acquisition of XANES data at Beijing Synchrotron Radiation Facility of Institute of High Energy Physics, CAS. This work was supported by National Natural Science Foundation of China (51272048) and the Ministry of Science and Technology of China (973 Program, 2013CB632402).

Notes and references

1 A. Fujishima and K. Honda, *Nature*, 1972, **238**, 37-38.
2 C. C. Chen, W. H. Ma and J. C. Zhao, *Chem. Soc. Rev.*, 2010, **39**, 4206-4219.
3 R. Asahi, T. Morikawa, T. Ohwaki, K. Aoki and Y. Taga, *Science*, 2001, **293**, 269-271.
4 Q. Kuang, X. Zheng and S. Yang, *Chem. Eur. J.*, 2014, **20**, 2637-2645.
5 M. R. Hoffmann, S. T. Martin, W. Y. Choi and D. W. Bahnemann, *Chem. Rev.*, 1995, **95**, 69-96.
6 X. J. Lang, W. H. Ma, C. C. Chen, H. W. Ji and J. C. Zhao, *Acc. Chem. Res.*, 2014, **47**, 355-363.
7 X. M. Zhou, G. Liu, J. G. Yu and W. H. Fan, *J. Mater. Chem.*, 2012, **22**, 21337–21354.
8 A. Tanaka, K. Hashimoto and H. Kominami, *J. Am. Chem. Soc.*, 2014, **136**, 586-589.
9 A. Kudo and Y. Miseki, *Chem. Soc. Rev.*, 2009, **38**, 253-278.
10 K. Maeda, K. Teramura, D. Lu, T. Takata, N. Saito, Y. Inoue and K. Domen, *Nature*, 2006, **440**, 295.
11 X. B. Chen, S. H. Shen, L. J. Guo and S. S. Mao, *Chem. Rev.*, 2010, **110**, 6503-6570.
12 F. E. Osterloh, *Chem. Soc. Rev.*, 2013, **42**, 2294-2320.
13 L. E. Stoflea, N. G. Apostol, C. Chirila, L. Trupina, R. Negrea, L. Pintilie and C. M. Teodorescu, *Journal of Materials Science*, 2014, **49**, 3337-3351.
14 S. Li, J. M. Zhang, M. G. Kibria, Z. T. Mi, M. Chaker, D. L. Ma, R. Nechache and F. Rosei, *Chem. Commun.*, 2013, **49**, 5856-5858.
15 A. Hagfeldt and M. Grätzel, *Chem. Rev.*, 1995, **95**, 49-68.
16 Y. Q. Qu and X. F. Duan, *Chem. Soc. Rev.*, 2013, **42**, 2568-2580.
17 R. G. Li, F. X. Zhang, D. G. Wang, J. X. Yang, M. R. Li, J. Zhu, X. Zhou, H. X. Han and C. Li, *Nat. Commun.* , 2013, **4**, 1432.
18 C. R. Bowen, H. A. Kim, P. M. Weaver and S. Dunn, *Energy Environ. Sci.*, 2014, **7**, 25-44.
19 L. Li, P. A. Salvador and G. S. Rohrer, *Nanoscale*, 2014, **6**, 24-42.
20 C. Hengky, X. Moya, N. D. Mathur and S. Dunn, *RSC Adv.*, 2012, **2**, 11843–11849.
21 M. Stock and S. Dunn, *J. Phys. Chem. C*, 2012, **116**, 20854-20859.
22 S. Park, C. W. Lee, M. G. Kang, S. Kim, H. J. Kim, J. E. Kwon, S. Y. Park, C. Y. Kang, K. S. Hong and K. T. Nam, *Phys. Chem. Chem. Phys.*, 2014, **16**, 10408-10413.
23 Z. Z. Lou, B. B. Huang, Z. Y. Wang, X. C. Ma, R. Zhang, X. Y. Zhang, X. Y. Qin, Y. Dai and M. H. Whangbo, *Chem. Mater.*, 2014, **26**, 3873-3875.
24 X. Fan, L. Zang, M. Zhang, H. Qiu, Z. Wang, J. Yin, H. Jia, S. Pan and C. Wang, *Chem. Mater.*, 2014, **26**, 3169-3174.
25 C. T. Campbell, *Top. Catal.*, 2013, **56**, 1273-1276.
26 V. Subramanian, E. E. Wolf and P. V. Kamat, *J. Am. Chem. Soc.*, 2004, **126**, 4943-4950.
27 S. Chen, J. Duan, M. Jaroniec and S. Z. Qiao, *Adv. Mater.*, 2014, **26**, 2925-2930.
28 Y. Li and G. A. Somorjai, *Nano Lett.*, 2010, **10**, 2289-2295.
29 H. G. Yang, C. H. Sun, S. Z. Qiao, J. Zou, G. Liu, S. C. Smith, H. M. Cheng and G. Q. Lu, *Nature*, 2008, **453**, 638-641.
30 Y. Yin and D. Talapin, *Chem. Soc. Rev.*, 2013, **42**, 2484-2487.
31 H. Tong, S. X. Ouyang, Y. P. Bi, N. Umezawa, M. Oshikiri and J. H. Ye, *Adv. Mater.*, 2012, **24**, 229-251.

32 X. M. Zhou, J. Y. Lan, G. Liu, K. Deng, Y. L. Yang, G. J. Nie, J. G. Yu and L. J. Zhi, *Angew. Chem. Int. Ed.*, 2012, **51**, 178-182.

33 X. Zhou, Q. Xu, W. Lei, T. Zhang, X. Qi, G. Liu, K. Deng and J. Yu, *Small*, 2014, **10**, 674-679.

34 J. Pan, G. Liu, G. Q. Lu and H. M. Cheng, *Angew. Chem. Int. Ed.*, 2011, **50**, 2133-2137.

35 A. Selloni, *Nat. Mater.* , 2008, **7**, 613-615.

36 Y. P. Bi, S. X. Ouyang, N. Umezawa, J. Y. Cao and J. H. Ye, *J. Am. Chem. Soc.*, 2011, **133**, 6490-6502.

37 Z. Jiao, Y. Zhang, H. Yu, G. Lu, J. Ye and Y. Bi, *Chem. Commun.*, 2013, **49**, 636-638.

38 D. J. Martin, N. Umezawa, X. Chen, J. Ye and J. Tang, *Energy Environ. Sci.*, 2013, **6**, 3380–3386.

39 T. T. Zhang, K. Zhao, J. G. Yu, J. Jin, Y. Qi, H. Q. Li, X. J. Hou and G. Liu, *Nanoscale*, 2013, **5**, 8375-8383.

40 M. A. Peña and J. L. G. Fierro, *Chem. Rev.*, 2001, **101**, 1981-2018.

41 L. Vayssieres, C. Sathe, S. M. Butorin, D. K. Shuh, J. Nordgren and J. H. Guo, *Adv. Mater.*, 2007, **17**, 2320-2323.

42 S. K. Mohapatra, S. E. John, S. Banerjee and M. Misra, *Chem. Mater.*, 2009, **21**, 3048-3055.

43 K. W. Urban, *Science*, 2008, **321**, 506-510.

44 C. L. Jia, S. B. Mi, K. Urban, I. Vrejoiu, M. Alexe and D. Hesse, *Nat. Mater.* , 2008, **7**, 57-61.

45 S. Kim, J. H. Lee, J. Lee, S. W. Kim, M. H. Kim, S. Park, H. Chung, Y. I. Kim and W. Kim, *J. Am. Chem. Soc.*, 2013, **135**, 6-9.

46 J. Y. Lan, X. M. Zhou, G. Liu, J. G. Yu, J. C. Zhang, L. J. Zhi and G. J. Nie, *Nanoscale*, 2011, **3**, 5161-5167.

47 Q. P. Ding, Y. P. Yuan, X. Xiong, R. P. Li, H. B. Huang, Z. S. Li, T. Yu, Z. G. Zou and S. G. Yang, *J. Phys. Chem. C*, 2008, **112**, 18846-18848.

48 L. Douillardt, F. Jollett, C. Bellint, M. Gautiert and J. P. Duraudj, *J. Phys.: Condens. Matter*, 1994, **6**, 5039-5052.

49 S. J. Pennycook and D. E. Jesson, *Phys. Rev. Lett.*, 1990, **64**, 938-941.

50 Y. Sun, L. Zhao, H. L. Pan, X. Lu, L. Gu, Y. S. Hu, H. Li, M. Armand, Y. Ikuhara, L. Q. Chen and X. J. Huang, *Nat. Commun.*, 2013, **4**, 1870.

51 P. L. Galindo, S. Kret, A. M. Sanchez, J. Y. Laval, A. Yanez, J. Pizarro, E. Guerrero, T. Ben and S. I. Molina, *Ultramicroscopy*, 2007, **107**, 1186-1193.

52 P. Galindo, J. Pizarro, S. Molina and K. Ishizuka, *Microsc. Anal.*, 2009, **23**, 23-25.

53 J. Shi, I. Grinberg, X. Wang and A. M. Rappe, *Phys. Rev. B*, 2014, **89**, 094105.

54 L. Y. Li, Z. F. Gan, M. R. McCartney, H. S. Liang, H. B. Yu, W. J. Yin, Y. F. Yan, Y. H. Gao, J. B. Wang and D. J. Smith, *Adv. Mater.*, 2014, **26**, 1052-1057.

55 Y. F. Cui, J. Briscoe and S. Dunn, *Chem. Mater.*, 2013, **25**, 4215-4223.

56 Y. Hong, J. Zhang, X. Wang, Y. Wang, Z. Lin, J. Yu and F. Huang, *Nanoscale*, 2012, **4**, 2859-2862.

57 R. Munprom, P. A. Salvador and G. S. Rohrer, *Chem. Mater.*, 2014, **26**, 2774-2776.

Table of contents

1D perovskite-type orthorhombic $KNbO_3$ nanowires display about two-fold as large as monoclinic counterparts toward RhB photodegradation and a synergy between ferroelectric polarization and electronic structure in photoreactivity enhancement is uncovered.